Cell Reports
Physical Science

CellPress
OPEN ACCESS

Article

# Nose-to-Brain Translocation and Cerebral Biodegradation of Thin Graphene Oxide Nanosheets

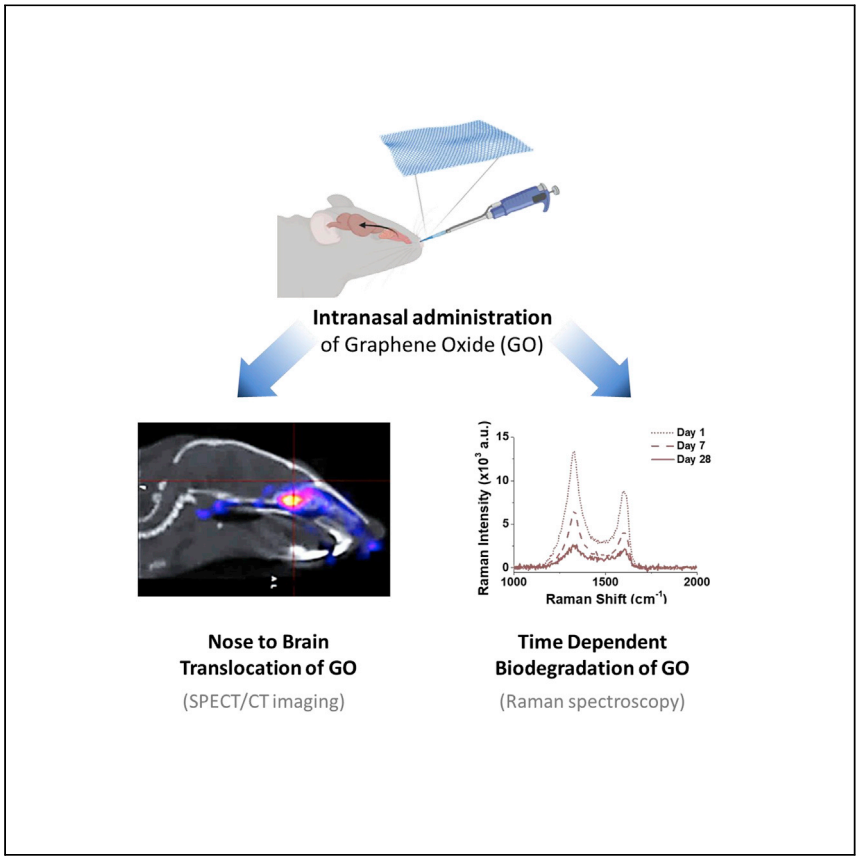


Depending on their applications, graphene-based materials may be inhaled. After exposing mice via the nasal cavity, Newman et al. demonstrate that thin graphene oxide sheets can infiltrate several brain regions in a size-dependent fashion. They show that the materials gradually experience changes consistent with biodegradation in the brain.

Leon Newman, Artur Filipe Rodrigues, Dhifaf A. Jasim, ..., Alberto Bianco, Cyrill Bussy, Kostas Kostarelos

cyrill.bussy@manchester.ac.uk (C.B.)
kostas.kostarelos@manchester.ac.uk (K.K.)

## HIGHLIGHTS

Thin graphene oxide sheets can translocate from the nasal cavity to the brain

Translocation is size dependent, with ultrasmall nanometric sheets translocating the most

Kinetics of graphene oxide accumulation are time dependent and brain-region-specific

Brain-accumulated graphene oxide undergoes changes consistent with biodegradation

Newman et al., Cell Reports Physical Science 1, 100176
September 23, 2020 
https://doi.org/10.1016/j.xcrp.2020.100176

Cell Reports
Physical Science

CellPress
OPEN ACCESS

Article

# Nose-to-Brain Translocation and Cerebral Biodegradation of Thin Graphene Oxide Nanosheets

Leon Newman,[1,2] Artur Filipe Rodrigues,[1,2] Dhifaf A. Jasim,[1,2] Isabella Anna Vacchi,[3] Cécilia Ménard-Moyon,[3] Alberto Bianco,[3,6] Cyrill Bussy,[1,2,*] and Kostas Kostarelos[1,2,4,5,7,*]

## SUMMARY

**Understanding the interactions of graphene oxide (GO)-based materials with biological systems is critical due to the potential applications of these materials. Here, we investigate the extent to which single- to few-layer GO sheets of different controlled lateral dimensions translocate from the nose to the brain following intranasal instillation. We explore tissue location and *in vivo* biodegradability of the translocated materials using various techniques. Mass spectrometry and confocal Raman analyses indicate that trace amounts of GO undergo nose-to-brain translocation in a size-dependent manner. The smallest GO-sheet size category (us-GO, 10-550 nm) gains the greatest access to the brain in terms of quantity and coverage. Confocal Raman mapping and immunofluorescence combinations show that *in vivo*, us-GO resides in association with microglia. Point-and-shoot Raman spectroscopy shows that trace quantities of us-GO are maintained over 1 month, but undergo biodegradation-related changes. This study adds to growing awareness regarding the fate of graphene-based materials in biological systems.**

## INTRODUCTION

Graphene is a two-dimensional (2D) sheet of $sp^2$-hybridized carbon atoms, and the archetypal member of the carbon nanomaterial (CNM) family[1,2]; since its characterization,[3] many graphene-based materials (GBMs), including single- to few-layer graphene oxide (GO) sheets and graphene quantum dots have been described.[4] GBMs continue to receive considerable attention due to their unique properties.[1,2]

GO is the main oxidized derivative of graphene.[5] It has been studied in various applications, including chemically resistant coatings with anti-corrosive properties,[6] membranes for tunable sieving of ions,[7] energy storage,[8] construction materials,[9] and biomedical technologies.[10,11] Workers in the chemical and manufacturing industries using or developing GO-containing products or products that require the use of GO, may be at risk of exposure. Larger populations may also be exposed if GO is incorporated into materials used in water treatment[12] or construction.[9] With increased research into the use of GBMs such as GO, the gap between bench-top research and consumer products is closing, making studies that seek to understand the biological interactions of these materials critical.[13] Such studies can help guide the production of safer GBMs by identifying physicochemical features that may make such materials hazardous, especially after inhalation, and should be avoided in their design.

[1]Nanomedicine Lab, Faculty of Biology, Medicine, and Health, The University of Manchester, AV Hill Building, Manchester, UK

[2]National Graphene Institute, The University of Manchester, Manchester, UK

[3]CNRS, Immunology, Immunopathology and Therapeutic Chemistry, UPR3572, University of Strasbourg, ISIS, 67000 Strasbourg, France

[4]Catalan Institute of Nanoscience and Nanotechnology (ICN2) and The Barcelona Institute of Science and Technology (BIST), Campus UAB, Bellaterra, Barcelona, Spain

[5]Twitter: @NanomedicineLab

[6]Twitter: @BiancoTeam

[7]Lead Contact

*Correspondence: cyrill.bussy@manchester.ac.uk (C.B.), kostas.kostarelos@manchester.ac.uk (K.K.)

https://doi.org/10.1016/j.xcrp.2020.100176

The nasal route represents a means by which nanomaterials can gain access to the brain in exposed individuals.[14] Per the International Commission on Radiological Protection (ICRP) model of fractional depositions of inhaled particles,[15] the aerodynamic diameter of an inhaled particle can influence its deposition in the pulmonary tract. Nanometer-sized particles are expected to deposit predominantly in the nasopharyngeal and laryngeal regions. Considering the anatomy of the olfactory region in the nose, which connects directly and indirectly with the brain,[16] nanoparticle deposition in this region may result in nose-to-brain translocation. In support of this, epidemiologic studies, clinical trials, and animal experiments exploring the biodistribution of inhaled nanoparticles have identified the materials in extrapulmonary organs, including the brain.[17–19] Several studies have examined the fate of GBMs in the pulmonary system[20–22]; however, none to date have explored the fate of the materials in the brain following potential nose-to-brain translocation.

Vulnerability of the central nervous system (CNS) to engineered nanoparticles was demonstrated initially by De Lorenzo and Darin[23]; gold particles were imaged in transit from the nasal mucosa to the brain using electron microscopy. Nose-to-brain transport is now an established phenomenon reported for a variety of nanoparticles, including silver nanoparticles,[24] iron oxide nanoparticles,[25] ultrafine carbon particles,[26] titanium dioxide nanoparticles,[27] manganese oxide nanoparticles,[28] and exosomes.[29] Recently, exogenous combustion-derived iron oxide nanoparticles were detected in the brains of deceased humans, previously living in distinctive geographic locations[30]; this presence in the CNS may have been the result of nose-to-brain translocation following inhalation of polluted air.[30]

Several modes of transport by which nanoparticles may enter the brain from the nasal cavities have been considered, including transport via axons of olfactory (olfactory neural pathway)[31] and trigeminal (trigeminal pathway)[32,33] neurons or via spaces between neuronal axons (paracellular transport).[34] Other pathways include paracellular or transcellular transport in relation to olfactory sustentacular epithelial cells.[16,35,36] Nanoparticles may also undergo absorption into the systemic circulation and then permeate the blood-brain barrier (BBB) to access the brain.[16] The latter pathway remains unlikely due to various defenses of a healthy BBB, including efflux pumps and narrow tight junctions.[37,38]

Here, we describe a study in which mice were exposed intranasally to aqueously dispersed GO sheets of different lateral dimensions (large- [l], small- [s], and ultrasmall- [us] GO). Our objectives were to understand (1) the influence of GO sheet lateral dimensions on the extent of nose-to-brain translocation and (2) the biodegradability of translocated materials over a 1-month period. Our hypothesis was that lateral dimensions of GO sheets would primarily govern the extent to which the materials underwent nose-to-brain translocation and that translocated GO sheets would be biodegraded by resident phagocytic immune cells. Recent studies have shown that CNMs, including GO, can undergo biologically mediated degradation, both *in vivo*[39–43] and *in vitro*.[44–46]

We show that single- to few-layer GO sheets undergo size-dependent nose-to-brain translocation following intranasal administration in mice, with us-GO achieving the greatest amount and coverage. Once in the brain, us-GO undergoes changes that are consistent with biodegradation, suggesting that its presence within the brain is likely to be transient.

## RESULTS

### Physicochemical Characterization of GO Materials

GO sheets of differing controlled lateral dimensions (l-GO, s-GO, and us-GO) were prepared by a modified Hummers' method under pyrogen-free conditions.[47,48] Structural characterization by transmission electron microscopy (TEM) and atomic force microscopy (AFM) (Figure 1A) revealed that each material (l-GO, s-GO, and us-GO) was composed of sheets of distinct lateral dimensions (Figure 1B). Further material characterization is provided in Figures S1 and S2. While l-GO sheet lateral dimensions were 1–35 μm, s-GO sheet lateral dimensions were 29 nm–1.9 μm, and us-GO sheets had a narrower size distribution, with lateral dimensions ranging from 10 to 550 nm. Other physicochemical parameters, such as oxidation degree and thickness, remained constant and comparable between the three sheet categories, permitting lateral dimension-based study.

To track and quantify the presence of GO after instillation, we functionalized GO sheets with a chelating agent (mechanism shown in Figure S3) that could bind traceable metallic probes $^{111}$In or $^{115}$In. The chelation agent used was 1,4,7,10-tetraazacyclododecane-1,4,7,10-tetraacetic acid (DOTA), attached to a poly(ethylene)$_4$ glycol molecule, which displayed a free amine group ($NH_2$-$PEG_4$-DOTA). There was a reduction in sheet lateral dimensions upon functionalization with $NH_2$-$PEG_4$-DOTA to form GO-DOTA ($PEG_4$ linker is not included in the name of the functionalized material for simplicity). The decrease in lateral dimensions was most evident for l-GO-DOTA in relation to the dimensions of l-GO; there was at least a 5-fold reduction. AFM showed that the thickness of GO materials had increased slightly upon DOTA functionalization (Figures 1A and 1B). Lateral dimension and thickness distribution histograms of the GO-DOTA structures are shown in Figure S1. Raman spectroscopy (Figures 1B and S2) revealed no significant changes in the I(D):I(G) ratio following functionalization. Fourier-transform infrared spectroscopy (FTIR) demonstrated new bands at 2,950–2,850 $cm^{-1}$, an increased band at ~1,600–1,650 $cm^{-1}$, and the presence of a stronger band at 1,260–1,330 $cm^{-1}$ for $NH_2$-$PEG_4$-DOTA compared with FTIR spectra of the starting materials. X-ray photoelectron spectroscopy (XPS) analysis demonstrated a decrease in the amount of epoxide groups and the added presence of C–N bonds on the GO sheets, following DOTA functionalization (Figure S2).

### Chelation and Stability of GO-DOTA[In] Conjugates

GO-DOTA materials were examined for their ability to chelate the metal isotopes radioactive $^{111}$In and non-radioactive $^{115}$In. We confirmed via radio-thin-layer chromatography (TLC) that after the chelation reaction using $^{111}$In, followed by 2 washing steps and compared with the control DOTA [$^{111}$In], chelation had occurred. A small amount of unbound DOTA[$^{111}$In] (~10%–13%) was detectable at the solvent front (Figure 2A). Inductively coupled plasma-mass spectrometry (ICP-MS) analysis indicated that GO-DOTA structures could chelate 0.2–0.4 μmol $^{115}$In/mg of GO-DOTA (Figure 2B, left).

Stability (the amount of $^{115}$In released over time compared with the initial amount of $^{115}$In chelated, shown in Figure 2B, right) of the GO-DOTA[$^{115}$In] constructs was assessed over time in 50% FBS at 37°C, at 1 and 7 days post-chelation using ICP-MS (Figure 2B, right). Similar to the radio-TLC results, at day 1, we observed a small free fraction of unbound DOTA [$^{115}$In] in the supernatant for each construct. Taking this into account, the GO-DOTA[$^{115}$In]-labeled complexes were 75%–80% stable, and at day 7 post-chelation; this stability was retained.

A

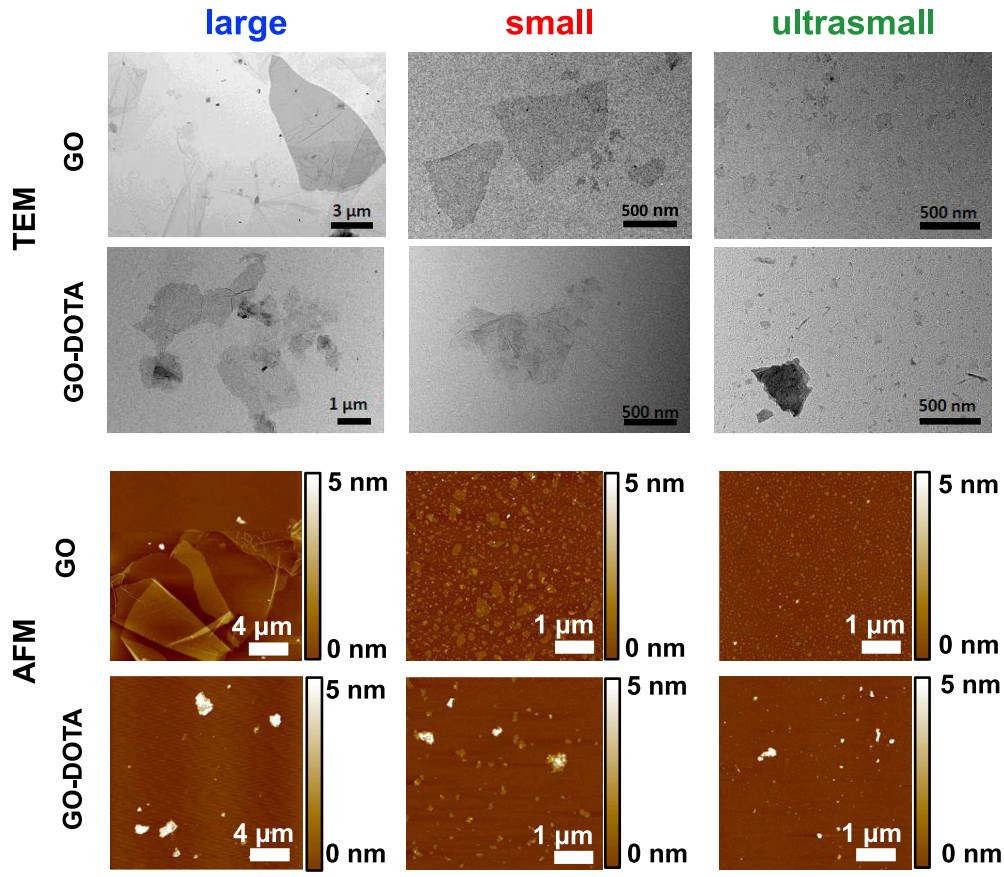


B

| *Parameter* | *Technique* | *l-GO* | *s-GO* | *us-GO* |
|---|---|---|---|---|
| *Lateral Dimension* | TEM | 10 μm [1–35 μm] | 450 nm [0.2–1.9 μm] | 122 nm [10–550 nm] |
| | AFM | 21 μm [10–30 μm] | 74 nm [29–369 nm] | 69 nm [30–300 nm] |
| *Thickness* | AFM | 1.8 nm [1–6 nm] | 2 nm [0.5–12 nm] | 1 nm [0.4–2.5 nm] |
| *I (D)/I (G)* | Raman | 1.30 ± 0.04 | 1.35 ± 0.02 | 1.34 ± 0.03 |
| *Parameter* | *Technique* | *l-GO-DOTA* | *s-GO-DOTA* | *us-GO-DOTA* |
| Lateral Dimension | TEM | 2 μm [0.2–5.1 μm] | 354 nm [29–1434 nm] | 160 nm [10–538 nm] |
| | AFM | 0.36 μm [0.1–3.5 μm] | 91 nm [30–800 nm] | 49 nm [30–480 nm] |
| Thickness | AFM | 1.9 nm [0.3–51.2 nm] | 2.5 nm [0.2–34.3 nm] | 2.6 nm [0.2–48.0 nm] |
| I (D)/I (G) | Raman | 1.34 ± 0.05 | 1.33 ± 0.03 | 1.34 ± 0.02 |

**Figure 1. Physicochemical Characterization**

(A) GO nanomaterials were interrogated for morphological and structural features by TEM and AFM, before and after DOTA functionalization. Histogram analysis of lateral dimensions (TEM and AFM) and thickness (AFM) distributions are provided in Figure S1. Spectroscopic features were analyzed with Raman spectroscopy, FTIR, and XPS, as shown in Figure S2. Scale bars are as indicated.

(B) The characterization summary table shows measured sizes, expressed as means and ranges.

## Size-Dependent and Brain-Specific Biodistribution of GO following a Single Intranasal Instillation

Brain-specific biodistribution of 30 μg l-GO-DOTA[$^{111}$In], s-GO-DOTA[$^{111}$In], or us-GO-DOTA[$^{111}$In] following a single intranasal administration was determined by

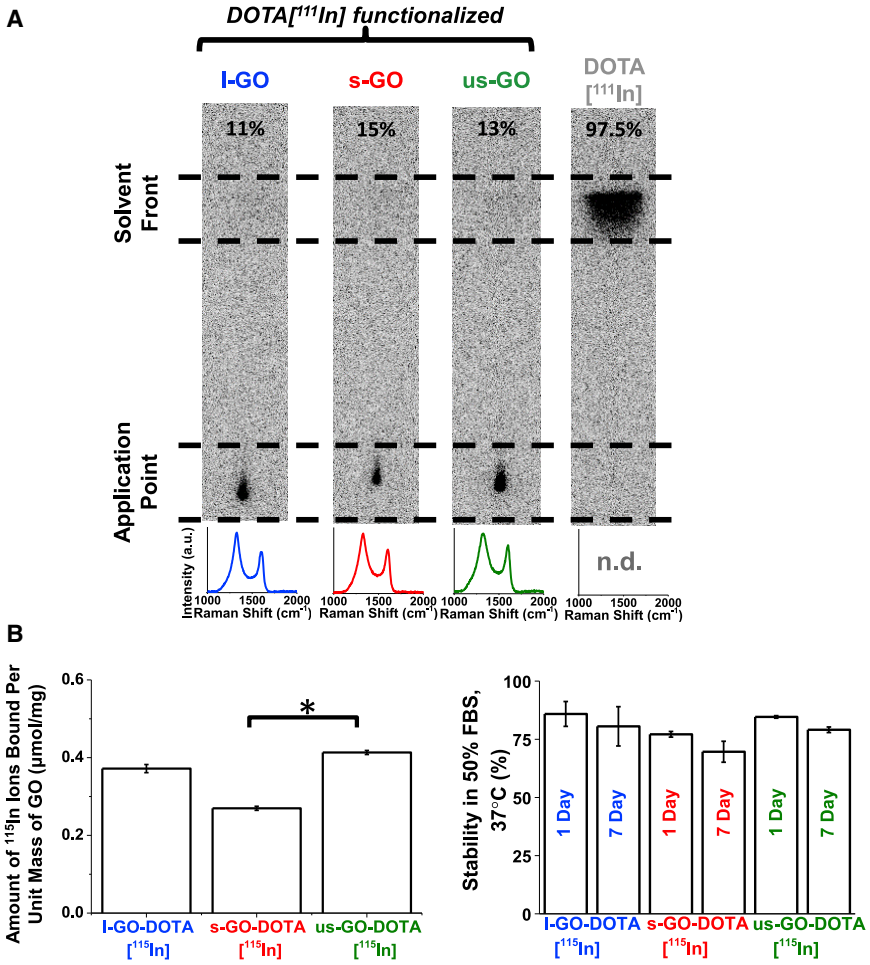


**Figure 2. Indium Chelation Efficiency and Stability of GO-DOTA[In] Conjugates**

(A) The chelation of $^{111}$In by GO-DOTA was assessed using radio-TLC and Raman spectroscopy (spectra acquired at the application point); n.d., not detectable.

(B) Left: the extent of chelation of $^{115}$In by each GO-DOTA construct (μmol of $^{115}$In per mg of GO-DOTA) was assessed immediately after the chelation procedure using ICP-MS. Right: stabilities of the constructs were assessed over 1 and 7 days in 50% fetal bovine serum (FBS) at 37°C using ICP-MS (100% binding was taken from the values determined in the left panel). All ICP-MS experiments were completed with at least 3 replicates. Values are plotted as mean ± SD. Statistical differences were assessed using the Kruskal-Wallis test followed by Dunn's post hoc test. *$p < 0.05$.

single-photon emission computed tomography/computed tomography (SPECT/CT) imaging, autoradiography, and γ-scintigraphy (Figure 3).

Per the qualitative SPECT/CT results, upon intranasal instillation, the 3 radiolabeled-GO materials partially accumulated in the nasal cavities (Figure S4). Signal intensity continued to be detected within the nasal cavities for 24 h (Figure 3A). Raman spectroscopy on the extracted nasal cavities was performed in a separate experiment using non-functionalized GO starting materials, and confirmed the presence of GO in each case (Figure S5). Twenty-four hours after intranasal administration, a weak radiation signal was detectable in the region of the brain corresponding to the olfactory bulb in mice administered s-GO-DOTA[$^{111}$In], us-GO-DOTA[$^{111}$In], or DOTA[$^{111}$In]. In contrast, radiation signal in the brain was not obvious for mice administered l-GO-DOTA[$^{111}$In] (Figure 3A).

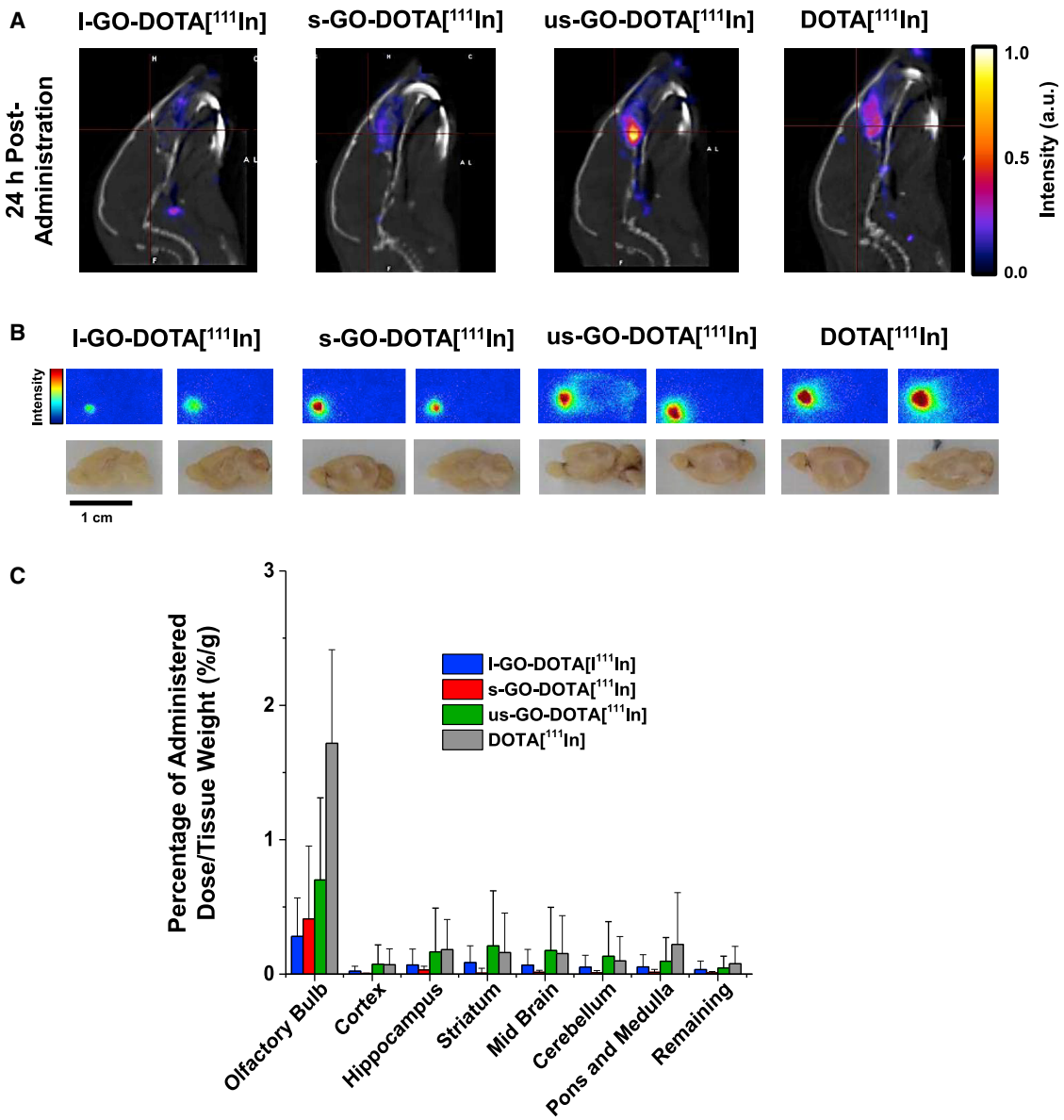


**Figure 3. Brain Biodistribution of GO-DOTA[In] Conjugates**

Biodistribution of GO-DOTA[$^{111}$In] was analyzed using (A) SPECT/CT imaging, (B) autoradiography of perfused, extracted, and immersion-fixed brains, and (C) γ-scintigraphy of microdissected perfused brain substructures. All scintillation values were subtracted from the background signal and are plotted as mean ± SD. Statistical significances were assessed using the Kruskal-Wallis multiple comparisons test with Dunn's post hoc test and were considered as $p < 0.05$; no comparisons met this criteria here. n = 3–4 mice were used per group.

Following SPECT/CT, animals were culled via cardiac perfusion and their brains (two mice per material) extracted, immersion fixed, and then sagittally sectioned into halves. The left half of each brain was placed onto an autoradiography plate for 7 days. The results demonstrated that all of the materials, including l-GO-DOTA [$^{111}$In], had undergone nose-to-brain translocation to some extent (Figure 3B). In agreement with SPECT/CT, the extent of translocation was least for l-GO-DOTA [$^{111}$In] and greatest for us-GO-DOTA[$^{111}$In]. The smallest us-GO-DOTA[$^{111}$In] had translocated to a comparable extent to DOTA[$^{111}$In]; both probes were detected in more than one brain region. It was not clear whether us-GO-DOTA[$^{111}$In] had

translocated to a greater extent compared with DOTA[$^{111}$In] or vice versa, due to the saturation of the signal observed in the autoradiography results and the low number of replicates. Noticeably, widespread diffusion was not apparent for mice treated with l-GO-DOTA[$^{111}$In] or s-GO-DOTA[$^{111}$In] (Figure 3B).

SPECT/CT and autoradiography results were validated quantitatively in a separate 24 h post-administration experiment by measuring the percentage of administered dose of l-GO-DOTA[$^{111}$In], s-GO-DOTA[$^{111}$In], or us-GO-DOTA[$^{111}$In] per gram of dried microdissected mice brain tissue, using γ-scintigraphy (Figure 3C). This technique was expected to reveal the weak radiation signals missed by previous techniques. Following intranasal administration of $^{111}$In-labeled GO-DOTA sheets, l-GO-DOTA[$^{111}$In] was again found to translocate to the least extent, while us-GO-DOTA[$^{111}$In] had the greatest translocation, and s-GO-DOTA[$^{111}$In] was in-between. The results of the group treated with DOTA[$^{111}$In] suggested that an even greater brain accumulation had occurred compared with us-GO-DOTA[$^{111}$In], although there was large intragroup variation.

Raman spectroscopy on homogenized brain tissues 24 h after instillation of non-functionalized GO sheets was used to confirm these biodistribution results. This approach allowed us to be more confident in rejecting the possibility that the radioactive signal used to locate GO sheets using previous techniques originated from free DOTA[$^{111}$In] and not the GO-DOTA[$^{111}$In] conjugates. It also helped to validate GO-DOTA as a suitable system to model the behavior of non-functionalized GO samples following intranasal administration. The results indicated that us-GO was present in all of the brain regions; s-GO in the olfactory bulbs, pons, medulla, and cerebellum; and l-GO in the olfactory bulbs, pons, and medulla (Figure 4).

### Cell-Specific Brain Distribution of us-GO 24 h following a Single Intranasal Instillation

The above results on GO brain biodistribution suggested independently that us-GO underwent the most extensive nose-to-brain translocation (albeit statistical significance was not achieved, likely due to the trace quantities and complex processing procedures; however, trends were apparent across all of the conducted experiments). Therefore, we focused our next experiments on the brain-specific localization and fate of us-GO in 2 regions, namely the olfactory bulb and cerebellum, at 24 h after intranasal administration. The pons and medulla were not chosen for this experiment due to difficulties in separating the structures from the spinal cord and cervical lymph nodes.

To investigate the cellular localization of us-GO, the brains of treated mice were cryo-sectioned and immunostained to identify three major brain cell types: microglia, astrocytes, and neurons (using anti-IBA-1, anti-GFAP, and anti-NeuN antibodies, respectively). To determine the potential presence of GO in or near these cells, confocal Raman mapping was conducted on the immunostained sections. Raman maps and immunofluorescence images were superimposed (Raman maps were made 50% transparent). Representative immunohistochemistry images with Raman overlay of olfactory bulb (Figure 5A) and cerebellum (Figure 5B) sections were provided. Due to the limited total number (n = 62) of GO Raman positive regions detected within brain sections across the 3 mice examined, only a semiquantitative representation is presented (Figure 5C). The data indicate that us-GO sheets were found predominantly in close association with microglia (Figure 5C).

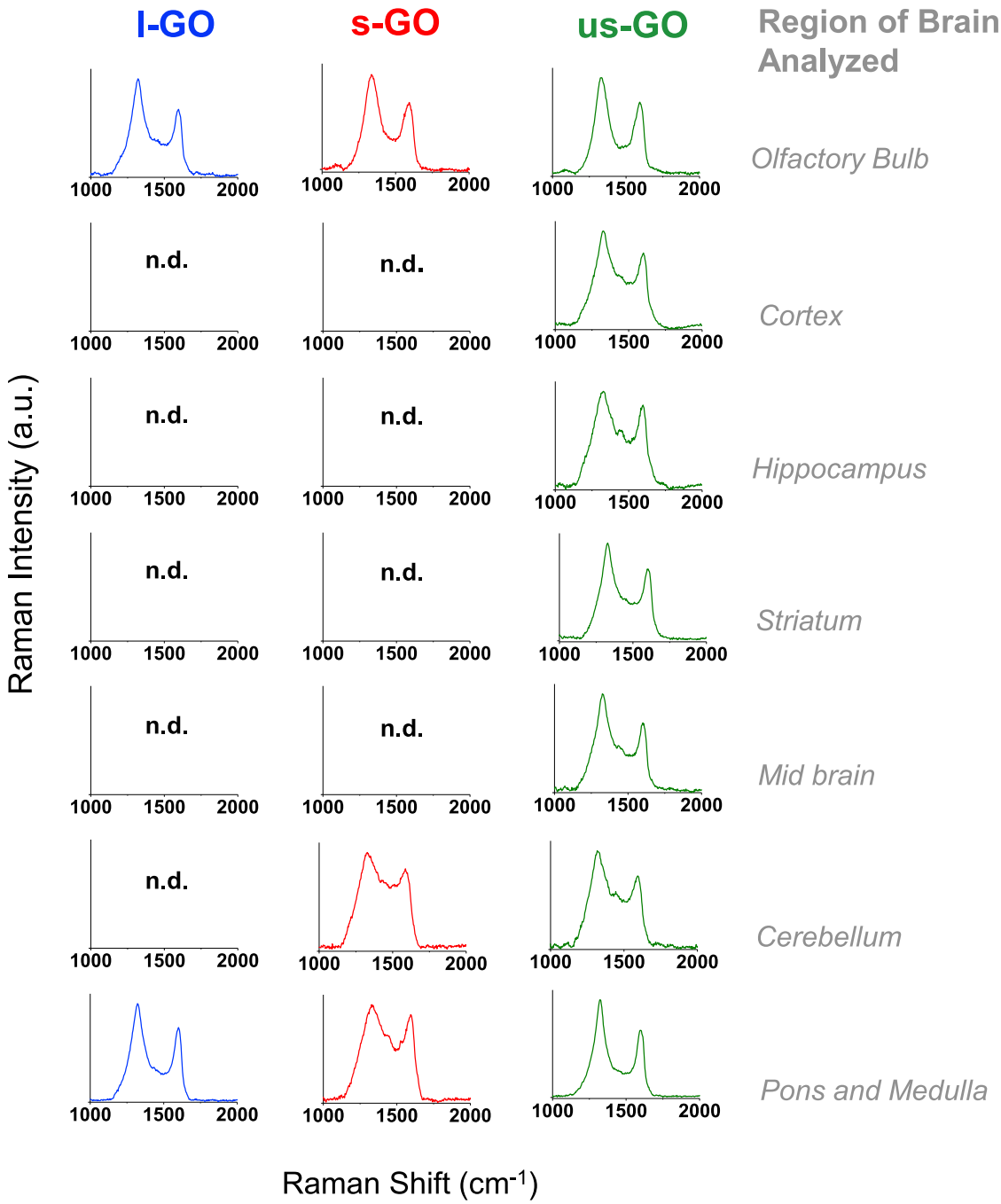


**Figure 4. Biodistribution of Non-functionalized GO in Brain Regions**

Each Raman spectrum is an average of 9 Raman spectra obtained from 9 different GO Raman positive regions, found across 3 mice. n.d., not detectable.

### Time-Dependent Distribution of us-GO at 1 and 7 Days following a Single Intranasal Instillation

We could not use γ-scintigraphy to assess the biodistribution of us-GO at time points after 24 h, due to the short radioactive half-life of $^{111}$In. Instead, we used the $^{115}$In isotope and measured the brain biodistribution of us-GO-DOTA[$^{115}$In] with ICP-MS, at days 1 and 7 post-administration. The results are presented in Figure 6 (percentage of administered dose per dry weight of tissue) and Figure S8

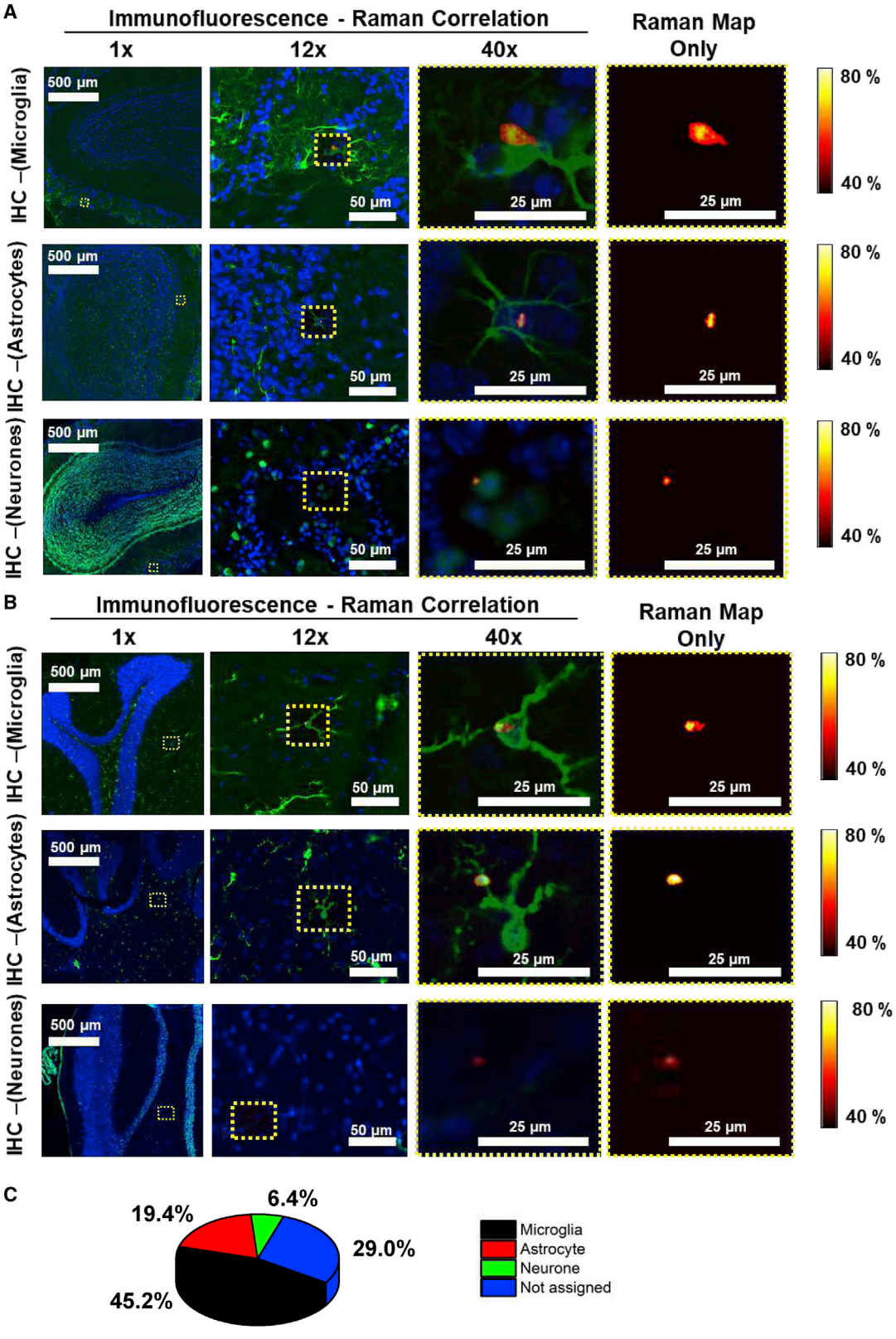

(percentage of administered dose per whole-brain substructure); results of this experiment confirmed those of the γ-scintigraphy experiment (Figure 3C). At 7 days, the overall amount of us-GO-DOTA[$^{115}$In] remained approximately the same. There were some variations when comparing each microdissected brain regions at days 1 and 7. At day 1, the DOTA[$^{115}$In] control exhibited a qualitative biodistribution similar to that of us-GO-DOTA[$^{115}$In]; however, the translocation to the olfactory bulb was much greater (Figure 6). Seven days after instillation, and in contrast to us-GO-DOTA[$^{115}$In], the vast majority of free DOTA[$^{115}$In] cleared from the brain; only traces were detectable within the cortex, hippocampus, and cerebellum.

To confirm the ICP-MS data by a technique that did not rely on a probe (i.e., $^{115}$In) but on GO intrinsic properties, we administered mice with non-functionalized us-GO and used Raman spectroscopy on the perfused and extracted brain sample homogenates. We obtained a qualitative Raman-based biodistribution at days 1 and 7, following intranasal administration of us-GO sheets (Figure 7). After 1 day, us-GO could be found in more than one brain region, as demonstrated previously (Figures 3, 4, and 6). After 7 days, us-GO was detected not only within the olfactory bulb and cerebellum in agreement with corresponding ICP-MS data but also in the pons and medulla.

### *In Vivo* Biodegradation of Nose-to-Brain-Translocated us-GO after Intranasal Instillation

To explore the *in vivo* fate of the translocated us-GO, biodegradation was assessed. We analyzed GO Raman spectra detected in brain homogenates to interrogate the crystalline state of the us-GO sheets over time (Figure 8). We focused this experiment on material present within the olfactory bulbs, where our data indicated that the majority of GO resided, and the cerebellum, where some material had further translocated. We extended the timeline of the experiment to 1 month to assess spectral changes more confidently. We detected GO at 3 different time points (days 1, 7, and 28) in both the olfactory bulb and cerebellum of treated mice (Figure 8A). GO Raman signal intensity decreased over time, and at 1 month, the signal intensity was at its minimum with respect to both brain regions. The rate at which the intensity decreased was greater for us-GO in the olfactory bulbs than in the cerebellum. With regard to the I(D):I(G) ratio at each time point, there was an initial increase in the ratio in the first 7 days in the olfactory bulb, whereas the ratio remained largely unchanged within the cerebellum (Figure 8B). At 1 month, however, there was a statistically significant decrease in the ratio for both regions compared with day 7.

We then assessed whether the same changes would occur if the same dose of us-GO were administered multiple times (5 doses over 5 consecutive days, 1 dose per day). There was only a modest increase in the number of GO$^+$ cells per square millimeter of brain tissue in both the olfactory bulbs and cerebellum following repeated

**Figure 5. Cellular Location of Non-functionalized us-GO within the Brain**

(A and B) Representative fluorescence images of brain cells (green indicates IBA-1$^+$ microglia, GFAP$^+$ astrocytes, or NeuN$^+$ neurons; DAPI (blue) was used to indicate cell nuclei), with Raman overlay (50% transparency) of tissue sections taken from (A) olfactory bulbs and (B) cerebellums of perfused brains of treated mice. The magnifications (12× and 40×) of regions of interest highlight the location of GO, as detected by overlaid 50% transparent Raman maps. Respective non-transparent 40× magnified Raman maps have been provided for comparison, with a color scale bar referring to the percentage of similarity of the Raman$^+$ region to a GO reference spectrum, given in Figure S6. Diagrammatic representation of the overlay procedure is provided in Figure S7, for reference.

(C) Pie chart highlighting the location of detected us-GO$^+$ regions (n = 62) in terms of their relative position to cells; this represents a semiquantitative distribution of GO location in brain tissue, 24 h following administration.

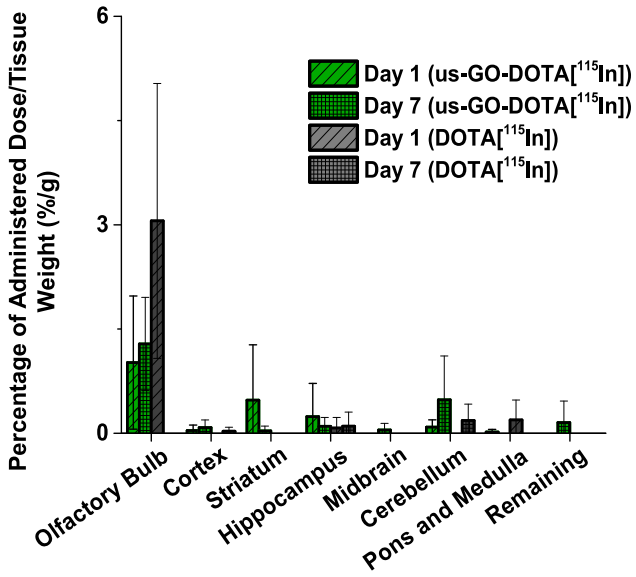


**Figure 6. Evolution of the Biodistribution of us-GO- DOTA[In] Conjugates from Days 1 to 7**

The biodistribution profiles of us-GO-DOTA[$^{115}$In] and DOTA[$^{115}$In] at days 1 and 7 was determined following a single intranasal administration. Each perfused microdissected brain region was analyzed with ICP-MS for the presence of $^{115}$In. The data are expressed as percentages of administered dose per weight (g) of dry tissue. The data corresponding to the average percentage of administered dose per anatomical brain region are presented in Figure S8. Values are plotted as mean ± SD. Statistical significances were assessed using the Kruskal-Wallis multiple comparisons test with Dunn's post hoc test and were considered as $p < 0.05$; no comparisons met this criteria here. n = 4 mice were used per group.

exposures compared with the single administration (Figure S9). We did not collect spectra for I(D):I(G) ratio determination at day 1 post-administration in this multiple-exposure experiment, as this would require more animals and because the predominant changes in the I(D):I(G) were previously observed to occur between days 7 and 28. Moreover, the I(D):I(G) ratio at days 7 and 28 could be compared with the I(D):(G) ratio of the materials at day 1 post-administration, as determined in the single-administration experiment. When analyzing Raman spectra in this multiple-exposure experiment (Figure S10), we observed an initial non-significant increase in the I(D):I(G) ratio at day 7 in mice administered multiple doses (compared with the ratio at day 1 as determined for us-GO, following administration with a single dose). Comparing the spectra obtained in the multiple-exposure experiment between days 7 and 28, we observed a decrease in the I(D):I(G) ratio and Raman signal intensity, in a fashion similar to the decrease found in the single-administration experiment.

### General Well-Being of the Mice during the Experiments

No change in body weight or signs of distress were found in mice treated with GO (Figure S11). They displayed normal behavior similar to those in the age-matched dextrose 5%-treated group (dextrose 5% was used here as the vehicle control [i.e., solution in which the GO was dispersed]).

## DISCUSSION

The notion that the lungs and other components of the respiratory tract are targets of inhaled nanoparticles has held strong; we recently revealed the impact of GO sheet size in this setting.[22] However, evidence from epidemiologic studies,[49] clinical

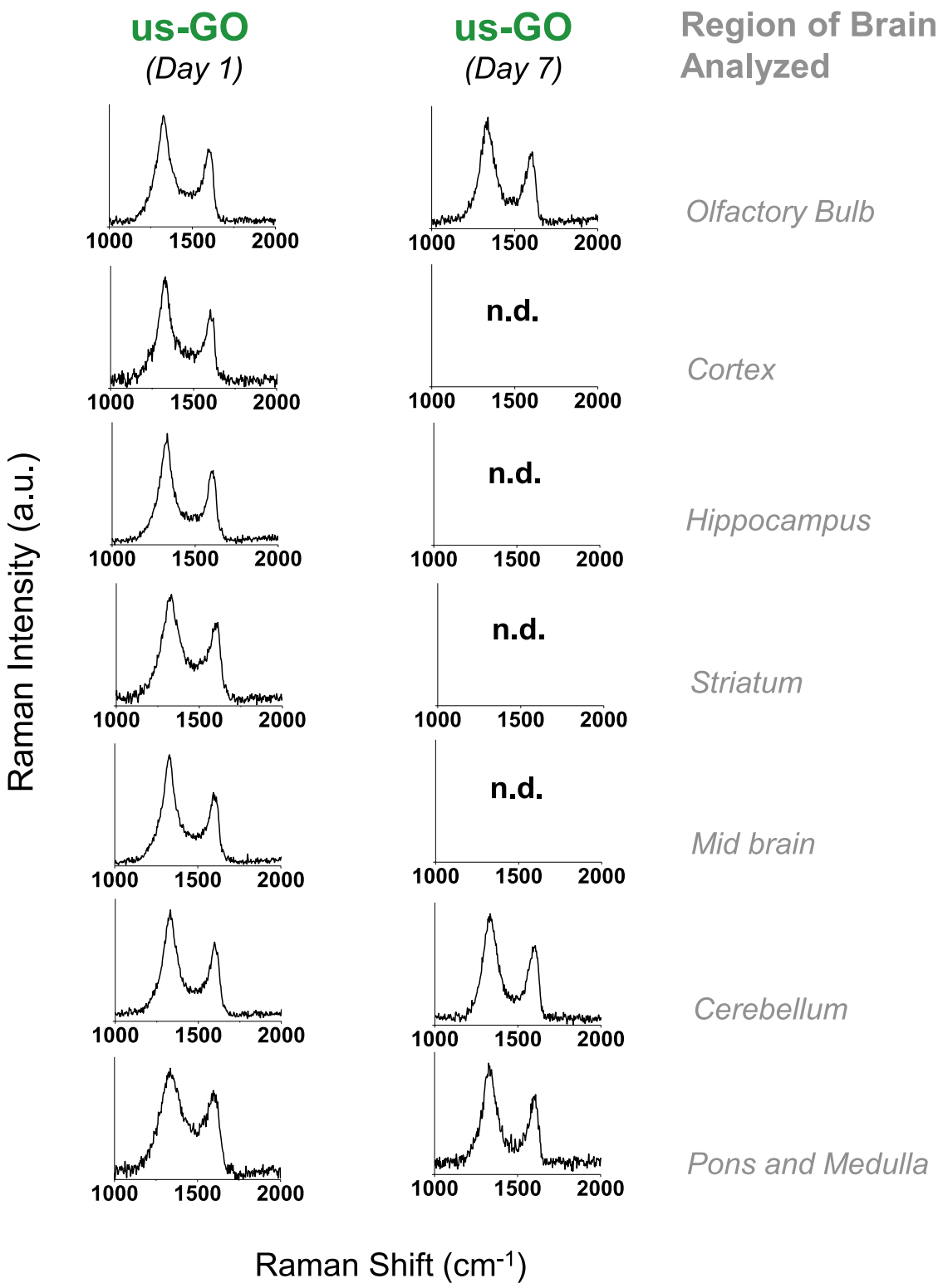


**Figure 7. Evolution of the Biodistribution of Non-functionalized us-GO from Days 1 to 7**

The presence of non-functionalized us-GO was confirmed in different perfused and microdissected brain regions using Raman spectroscopy. Each Raman spectrum is an average of 9 GO Raman$^{+}$ regions found across 3 mice at each condition and time point. n.d., not detectable.

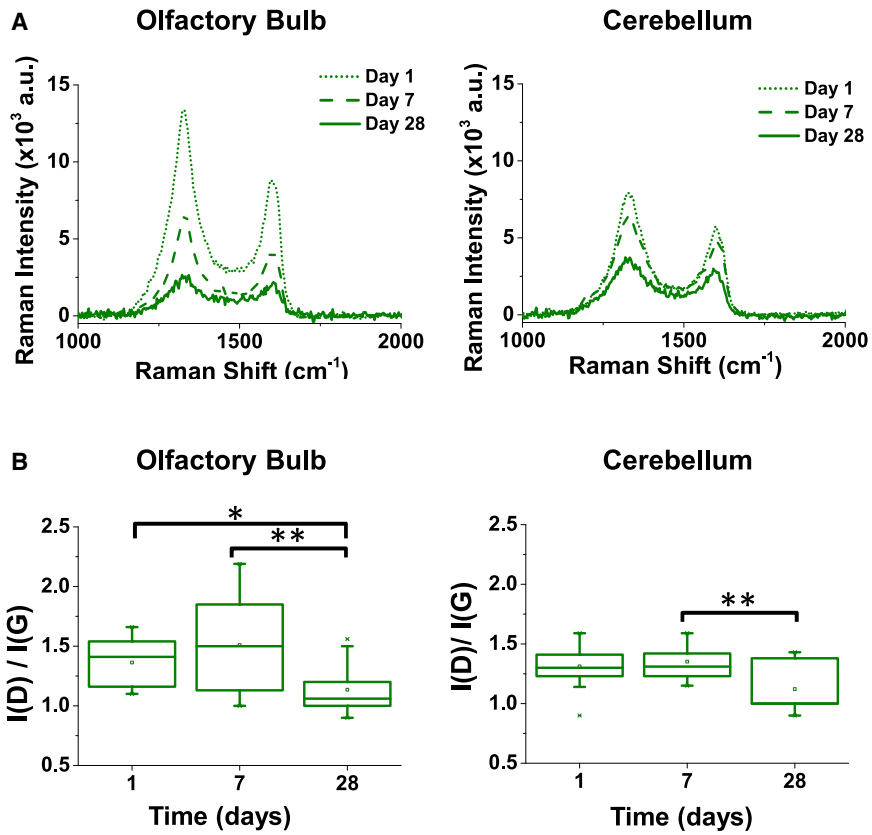


**Figure 8. Biodegradation of us-GO over 28 Days**

Olfactory bulbs (left) and cerebellums (right) of perfused brains of mice treated with us-GO were isolated, physically homogenized, and screened for the presence of GO, using Raman spectra at days 1, 7, and 28.

(A and B) Average Raman signal (A) and the boxplots (B) of the I(D):I(G) at each time point are presented. At each time point, 5 spectra were collected from each of the 3 mice treated. Values are plotted as mean ± SD. Statistical significances were assessed using a Kruskal-Wallis test with Dunn's post hoc test. *$p < 0.05$ and **$p < 0.01$.

trials,[50] and animal experiments[24] has shown that extrapulmonary organs including the brain can also be affected. Here, the potential of GO sheets of different controlled lateral dimensions to undergo nose-to-brain translocation following intranasal instillation was investigated.

To perform our investigation, DOTA-functionalized and non-functionalized GO materials were used. The purpose of the DOTA-functionalized materials was to allow the labeling of GO sheets with metallic probes that could facilitate their identification and quantification within tissues. Single- to few-layer GO sheets of controlled lateral dimensions[48] were functionalized with DOTA connected to a $PEG_4$ linker group ($NH_2$-$PEG_4$-DOTA) via an epoxide ring-opening reaction.[51] This strategy allowed the functionalization of GO materials, without disrupting the graphitic backbone or causing chemical reduction. We have shown that this epoxide ring-opening reaction is a versatile means to functionalize GBMs.[51] The lateral dimensions of the l-GO-DOTA sheets were smaller than that of the starting l-GO sheets. Changes in lateral dimensions were not as obvious for s-GO-DOTA or us-GO-DOTA compared with the respective non-functionalized materials. Nevertheless, the lateral

dimensions of l-GO-DOTA remained greater than that of s-GO-DOTA and us-GO-DOTA constructs, permitting a lateral dimension-based examination of the nose-to-brain translocation of GO sheets. The observation that a reduction in the lateral dimensions occurs in GO sheets following chemical functionalization has been previously reported by us[52] and others.[53]

The reduction in l-GO sheet lateral dimension may be a consequence of the cooperative alignment of epoxy groups, which is expected to create fracture lines in the sheets.[54,55] Upon epoxide ring-opening using the amine group of the $NH_2$-$PEG_4$-DOTA group as the nucleophile, a mass unzipping of the sheet along epoxide-related fracture lines could occur, resulting in graphene sheets of smaller lateral dimensions. This phenomenon was not observed to the same extent for s-GO or us-GO sheets. We hypothesize that the cooperative alignment of epoxy groups—the required configuration of epoxides for an unzipping process to occur—in these smaller and more numerous sheets was less likely, due to the smaller surface area and consequent fewer epoxide groups per individual us- or s-GO sheets, relative to individual l-GO sheets.

Sheet thickness was observed to increase on average for all sheet size categories upon DOTA functionalization and may be due to the added DOTA functionalities. Increased thickness has also been reported following the functionalization of GO with other DOTA derivatives,[52] dextran,[56] and PEG.[53] The graphitic backbone of the materials was interrogated using Raman spectroscopy, which demonstrated the presence of characteristic D and G scatter bands (~1,330 and ~1,595 $cm^{-1}$). The spectra of the materials were scrutinized for their I(D):I(G) ratio, which is used commonly to assess disorder within GBMs.[57] When comparing the I(D):I(G) ratios of GO sheets and GO-DOTA conjugates, the value of the ratio did not increase significantly, which was expected because of the conditions used in the epoxide ring-opening reaction.[51]

FTIR analysis revealed differences between the non-functionalized and DOTA-functionalized GO sheets, confirming the chemical modification. Compared with GO, GO-DOTA displayed enhanced and broader bands near 1,650 $cm^{-1}$ and at 1,260–1,330 $cm^{-1}$ in the regions where the amide C=O stretch, and C–N stretch and C–H bending are expected, respectively. There were also 2 new bands between 2,850 and 2,950 $cm^{-1}$, which were attributed to the stretching of aliphatic C–H groups. This supported the functionalization of GO with $NH_2$-$PEG_4$-DOTA, resulting in GO structures that contained N–H and C–N bonds and were rich in aliphatic C–H groups. XPS of the functionalized materials compared with the non-functionalized materials supported these inferences. Similar observations have been reported previously.[52,58]

Using radio-TLC, we demonstrated the successful retention of $^{111}In$ by GO-DOTA. Using ICP-MS, we show that all GO-DOTA materials chelated a comparable and significant amount of $^{115}In$. GO-DOTA[$^{115}In$] structures were shown to be 75%–80% stable when incubated in serum at 37°C, over 24 h. These values are comparable with those reported in previous studies.[59,60] No significant decreases in stability were detected for up to 7 days, indicating that this stability was maintained. We have shown previously that non-functionalized GO sheets labeled via simple mixing with free In ions result in structures that exhibit poor stability over time in serum at 37°C; the majority of bound In was released in 24 h.[52] The initial release in our current experiment was likely due to small amounts of unreacted $NH_2PEG_4$-DOTA, which may have been physisorbed onto the surface of the GO

and then released gradually over 24 h. Taken together, the physicochemical and labeling characterizations demonstrate the synthesis of GO-DOTA sheets of controlled lateral dimensions.

Alternative labeling strategies have been reported; these include labeling with radioactive iodine,[61] which requires no chelating agent-based attachment. These strategies often use highly oxidizing species, which can damage the graphitic backbone of the materials. Moreover, physiological accumulation of iodine within the thyroid gland can lead to difficult-to-interpret data.[56] Physical adsorption strategies to attach radioactive metals, bound within a chelating agent, onto the surface of GO via $\pi$-$\pi$ interactions have also been investigated. These strategies can result in large increases in sheet thickness,[62] potentially affecting the behavior of the materials and compromising their value as models to approximate the biodistribution of single- to few-layer GO sheets.[21,63]

Following successful preparation of labeled GO constructs of different controlled lateral dimensions, we investigated the materials' respective brain biodistribution profiles after intranasal administration. Qualitative SPECT/CT imaging data revealed that during the early time points (i.e., 30 min after instillation), there was no convincing evidence of transfer of materials across the cribriform plate, the structure that separates the CNS from the roof of the nasal cavities. After 3 h, a weak signal could be seen in the olfactory bulbs of mice administered with either us-GO-DOTA[$^{111}$In] or DOTA[$^{111}$In]. This provided evidence of the translocation of these two materials from the nasal cavities to the brain. Other studies investigating nose-to-brain transport of nanoparticles also reported a short delay between the time of administration and the translocation of materials to the brain.[64] This is possibly due to the size of the materials and nature of the translocation mechanisms. Based on the results of our multiple techniques, 24 h after administration, stronger evidence of the translocation of materials from the nose to the olfactory bulb was apparent in the s-GO-DOTA, us-GO-DOTA, and DOTA control groups. Other than SPECT/CT, all of the experiments were performed on animals sacrificed via cardiac perfusion; this reduced the possibility of signal originating from materials circulating in cerebral blood vessels.

The initial detection of materials within the olfactory bulb 3 h after a single administration suggests that it was unlikely that translocation occurred only via axonal transport. In this pathway, materials in the nasal cavities are taken up by neurons via endocytosis or pinocytosis and are actively transported through the cribriform plate in a retrograde fashion toward the olfactory bulb.[23,31,35] Axonal transport tends to be relatively slow; studies have shown that ~24 h is typically required before any material reaches the CNS.[65] Axonal transport may, in part, be responsible for some translocation of materials into the brain, particularly at 24 h, but it does not explain the initial rapid (within 3 h) transport found for us-GO. Another possibility is the transport of materials from various locations (e.g., nasal cavity, respiratory tract, stomach, intestine) after their translocation from the nasal cavity to the systemic circulation. From here, materials could cross the BBB and migrate into the CNS[36,37]; this mechanism is unlikely to explain our results, as the initial and major accumulation was observed within the olfactory bulb near the cribriform plate. This pattern of accumulation would not be expected had the materials entered the brain primarily by crossing the BBB. Moreover, previous biodistribution studies that used higher doses of GO showed that when administered systemically, the majority of materials underwent extensive urinary excretion, while the remnant fraction was taken up by components of the mononuclear phagocytic system such as the

spleen, with no obvious uptake into the brain.[52,66] Studies that investigated the transfer of intravenously administered GO from the systemic circulation to the brain showed that even at high dosages, there was negligible evidence of BBB permeation.[67,68] Other mechanisms of nose-to-brain transport include transcellular conveyance of materials through the olfactory sustentacular epithelial cells or paracellular transport through narrow tight junctions between these sustentacular epithelial cells.[16] These transport mechanisms can occur continuously over short time frames and are more likely to explain the rapid appearance of materials within the olfactory bulb. Drug molecules, fluorescence molecular tracers, exosomes, and quantum dots, when administered intranasally, have also been reported to translocate to the olfactory bulb within short time frames.[29,36,64,69–71]

SPECT/CT imaging, autoradiography maps, and γ-scintigraphy measurements, all using functionalized materials, together with the Raman-based biodistribution using non-functionalized materials, provide quantitative and qualitative matching evidence to support size-dependent nose-to-brain translocation of GO sheets. Size-restriction issues could explain these findings. De Lorenzo[31] determined that axons of olfactory neurons (in 2-month-old rabbits) had approximate diameters of 200 nm. This indicates that axonal transport would be permitted in similarly small mammals, only if the materials in question did not exceed the diameter of the neuronal axons. Transcellular transport through the olfactory sustentacular epithelial cells is also possible, but, again, will be size restricted due to the sizes and capacities of the cells involved. Paracellular diffusion pathways, between olfactory sustentacular cells and neurons, are also size limited. Tight junctions between cells of the olfactory mucosa are reported to be 3.9–8.4 Å, allowing negligible transport of materials >15 Å.[72] Even in the presence of absorption enhancers, these tight junctions will open by 15–20 times their normal size,[73] resulting in gaps below the nominal lateral dimensions identified during the characterization of the GO materials tested. However, frequent turnover of the olfactory neurons may provide opportunities for larger particles to penetrate.[74,75] Other studies have also reported that size plays a critical role in determining the extent that nanoparticles undergo nose-to-brain translocation.[29] Our findings may be relevant for industries that aim to produce water-stable 2D materials with safer (by design) features[76]; materials with lateral dimensions >1 μm may appear safer with respect to possible inhalation and brain exposure.

According to the ICRP model,[15] nanoparticles would be expected to remain lodged within the nasal cavities after intranasal administration.[77,78] To confirm this expectation, we harvested the nasal cavities from animals treated with non-functionalized GO 24 h after instillation. Black materials were found in or on the tissue (Figure S5). Raman-based analysis confirmed the graphitic nature of these black materials. The amount of material found in the nasal cavities 24 h post-administration was size dependent (as indicated also by the SPECT/CT imaging at 24 h post-administration); the lowest amount was observed visually in l-GO-treated animals and the highest in us-GO-treated animals. This may have contributed to the observed size-dependent nose-to-brain translocation.

After 24 h, besides being present in the olfactory bulbs, trace quantities of us-GO translocated to more distant structures, such as the cortex, striatum, hippocampus, midbrain, cerebellum, and the pons and medulla. Previous studies have also reported the presence of materials in distant brain structures following the intranasal administration of carbon particles,[26] iron oxide nanoparticles[79] and exosomes.[29] On close analysis of the sagittal autoradiography maps, us-GO appeared to reach these distal brain structures after passing through the olfactory bulb (as suggested by the

gradient from the olfactory bulb to distal regions) rather than being introduced by an alternative means. Extraneuronal transport pathways (i.e., in between cells) may explain this observation. These pathways may transport administered nanoparticles directly from the nasal epithelium and olfactory bulb regions into the cerebrospinal fluid within the subarachnoid space that surrounds the brain.[36] The materials may then move toward deeper sites in the brain by convective flow driven by arterial pulsations, through perivascular spaces[71,80] surrounding surface and brain-penetrating arteries before being released into the brain interstitial spaces.[81] The total quantity of GO that reached the brain in the present study was very low—on average ~0.012% of the initial dose. The dose of the material per gram of dry tissue in the olfactory bulb was higher than that in other studies using nanoparticles, such as 20 nm silver nanoparticles,[24] but comparable with that reported in studies using related materials, such as ultrafine carbon particles derived from graphite.[26] In all of the cases, the total quantity that translocated into the mice brains was far lower compared with values reported in studies exploring the use of nanoparticles for nose-to-brain drug delivery.[82] If larger mammals were to be exposed, then the nose-to-brain translocation of us-GO would be expected to be greater due to the higher absolute surface area of exposed nasal epithelium[83] and volume of air breathed in. However, there are several differences between mammalian species, including anatomy and physiology of airways that may influence the extent of this potential translocation.

We focused our subsequent experiments on us-GO-based structures, as us-GO-DOTA accumulated in the brain to the greatest extent at 24 h compared with the other GO structures. Using Raman map analysis in correlation with immunofluorescence microscopy, we investigated the location of us-GO sheets within the olfactory bulb and cerebellum, with respect to three main cell types in the brain. The olfactory bulb and cerebellum were selected for their distance apart. In both brain regions, most of the translocated material was associated with microglial cells, with smaller fractions associated with astrocytes, and less so with neurons. This suggested that us-GO sheets were able to translocate to the deep brain parenchyma, albeit in diminutive quantities, and interact with different brain cell populations. Microglial cells are the resident macrophages of the CNS and should be able to recognize us-GO sheets as foreign materials.[84,85] Sequestration of us-GO by microglial cells after intranasal administration and nose-to-brain transport has been previously reported for other nanomaterials, such as exosomes,[29] silver nanoparticles, and quantum dots.[24,64] Under certain conditions, the internalization of nanomaterials by macrophages has been associated with cytotoxic and inflammatory responses.[86,87] Further research is therefore warranted to assess the impact of us-GO accumulation in microglia and on brain physiology and functions, especially after repeated exposure and looking at possible delayed-onset reactions. In this respect, recent studies investigating the effect of direct stereotactic administration into the brain parenchyma of single- to few-layer GO sheets demonstrated that the materials were not associated with significant *in vivo* adverse effects.[88]

Following the initial entry of us-GO-DOTA into the brain, ICP-MS (detecting $^{115}$In) and γ-scintigraphy (detecting $^{111}$In) revealed similar brain regional distributions at day 1, with the highest accumulation in the olfactory bulb. When examining the 7-day time point, the overall percentage of the administered dose of the us-GO materials throughout the brain remained on average constant with non-significant variations. This was unlike the DOTA control, which had almost cleared from all of the brain regions by day 7, indicating that us-GO-DOTA sheets and free DOTA

evolved differently with regard to their distribution profiles, with greater retention of us-GO-DOTA in several brain regions. It also reaffirmed the stability of our materials *in vivo*. The similar biodistribution profile at day 1 supported the idea that us-GO-DOTA had traveled mostly through perivascular and interstitial spaces, where small molecules such as DOTA are also likely to gain access, permitting the flow and diffusion of materials and molecules from the olfactory bulb to more distal regions (e.g., the cerebellum) over time. It is possible that after 7 days, free DOTA, unlike us-GO-DOTA, had been cleared by mechanisms such as lymphatic transport.[80,89,90] These mechanisms are also relevant to materials in the interstitial space and not entrapped in cells.

An important question was whether this trace amount of translocated and brain-retained us-GO sheets could be biodegraded. This was an intriguing concept, as most of the material was shown to be associated with microglial cells, which are known to remove and degrade unwanted materials, including CNMs.[40,44] In a previous study,[43] we showed that *in vivo* degradation of GO sheets was plausible when GO materials interacted with cells with degradative capabilities.[42,91] In this previous study,[43] splenic macrophages sequestered GO sheets and mediated their structural degradation over a 9-month period. In the past, we have also demonstrated, *in vivo*[40] and *in vitro*,[44,46] that microglial cells can biodegrade $sp^2$-hybidized CNMs. These previous results are supported by several degradation studies that demonstrate the capacity of mammalian enzymes in this respect.[92,93]

Based on this knowledge, we used Raman spectroscopy to probe the crystalline state of the non-functionalized GO sheets[57] after their translocation to the brain. Within the olfactory bulb, GO-Raman signal intensity and integrity decreased gradually. The I(D):I(G) ratio increased from day 1 to day 7, indicating that the degree of defects had increased within the materials.[57] The Tuinstra-Koenig equation predicts that the I(D):I(G) ratio should increase in graphitic material until the material achieves maximum defect density, at which point, the ratio will decrease.[57] In line with this, after 1 month, the I(D):I(G) ratio decreased to a level below that of the starting materials. This signified an increase in defects and presence of amorphicity in the graphitic backbone of our brain-bound us-GO sheets. The continuation of such processes is expected to cause gradual attenuation of all of the component peaks associated with the Raman spectra of GO.[57,94] These results suggest that us-GO sheets, previously shown to be largely associated with microglial cells, underwent biodegradation-related changes in the brain, in agreement with other studies concerning the biodegradation of CNMs.[40,44–46,95] The exact mechanisms by which microglial cells degrade CNMs require further investigation, but may involve peroxidase family enzymes, NADPH oxidase, or other cell components, as reported for macrophages and neutrophils.[42,96–98] Results from the cerebellum indicate that GO materials underwent a similar transformation, albeit at a slower rate.

From a toxicological perspective, demonstrating that cells in the brain may be able to degrade trace quantities of us-GO sheets that translocate to the brain is a relieving prospect. It suggests that, even though us-GO sheets can enter the brain from the nasal cavities, their residence as non-degraded GO sheets may be transient, reducing the potential risk of long-term damage to brain tissue due to material persistence. To challenge the robustness of this statement, we conducted a multiple-exposure experiment (5 repeat administrations of the dose initially administered in the single-exposure experiment; 1 dose per day over 5 consecutive days). We

were surprised to find that there was only a modest increase in the amount of material deposited within the brain, perhaps due to the initial accumulation of GO in the nasal cavities, blocking further entry. Nevertheless, over the course of 1 month, the GO Raman signal evolved in a way similar to that observed after a single exposure, suggesting that biodegradative processes were occurring. Even though the persistence of us-GO sheets in the brain may be averted due to biodegradation, it is uncertain whether the transformed material would be cleared from the brain. More research is needed in this respect.

Previous studies have shown that *in vitro* enzyme-derived CNM degradation products do not induce enhanced toxic effects *in vivo* following pulmonary and peritoneal administration.[96,99] Throughout our experiments, we regularly measured the weights and observed the general well-being and body condition of all of the mice, in agreement with standards defined previously.[100] No abnormal weight loss or behaviors were observed relative to age-matched vehicle (dextrose 5%) control. These observations support the absence of the significant detrimental effects of translocated materials and biodegradation by-products. Further investigations should assess whether the observed trace amounts of materials and their degradation by-products can impair brain function and physiology, particularly at long term after exposure.

If graphene nanoplatelets of equal dimensions to us-GO were administered in mice using our methodology, then nose-to-brain translocation of these materials would likely be more limited due to their hydrophobicity and greater tendency to agglomerate compared with GO. In this respect, large agglomerates would not translocate to the brain easily due to size restrictions, as seen here with l-GO. If graphene sheets were to enter the brain, however, their biodegradation would likely be of a different kinetic profile, presumably significantly slower due to the lack of defects in the planar lattice of these materials. Previous studies have shown that enzymes involved in the biodegradation process interact preferentially with defected sites in CNMs to catalyze their degradation.[101] The possible long-term persistence and impact of graphene nanoplatelets entering the brain should, therefore, be explored further.

In conclusion, our results suggest that following the intranasal administration of aqueously dispersed GO sheets, the materials underwent size-dependent translocation to the brain. The smallest sheet size category (us-GO, 10–550 nm) experienced the greatest translocation and was present in every examined brain region, notably in the olfactory bulb. However, the percentage of materials that translocated to the brain is diminutive compared with the administered dose. Focusing on us-GO, we observed that a large fraction of the translocated material resided in association with the microglia. Over 1 month, us-GO sheets present in the brain were subjected to *in vivo* biodegradative processes, which were likely affecting the fraction associated with, or sequestered within, microglial cells. This study adds to the growing awareness regarding the potential interaction of GBMs with biological systems, which is critical in light of the predicted increase in the use of these materials.

## EXPERIMENTAL PROCEDURES

### Resource Availability

#### *Lead Contact*

Further information and requests for resources and reagents should be directed to the Lead Contact, Prof. Kostas Kostarelos (kostas.kostarelos@manchester.ac.uk).

*Materials Availability*

All unique/stable reagents generated in this study are available from the Lead Contact.

*Data and Code Availability*

All data associated with the study are included in this article and the Supplementary Information. Raw data are available from the Lead Contact on reasonable request.

### Synthesis of Non-functionalized GO Sheets of Differing Lateral Dimensions

The synthesis of GO sheets of controlled different lateral dimensions was in accordance with our protocol, as previously described.[48] During the procedure, measures were taken to minimize the contamination of GO with endotoxin, including the use of depyrogenated glassware, use of water for injection, and the handling of GO post-synthesis under sterile laminar flow cabinets.

### $PEG_4$-DOTA Functionalization of GO Sheets

$NH_2$-$PEG_4$-DOTA (9 mg, 0.0129 mmol) was added to an aqueous suspension of GO starting material (either us-GO, s-GO, or l-GO) (9 mg, 1 mg/mL). The mixture was left to react for 2 days under continuous stirring at room temperature. GO-DOTA was then directly dialyzed in MilliQ water for 4 days. The final GO-DOTA was stored in water, without further treatment. For further details, see the Supplemental Experimental Procedures.

## SUPPLEMENTAL INFORMATION

Supplemental Information can be found online at https://doi.org/10.1016/j.xcrp.2020.100176.

## ACKNOWLEDGMENTS

This work was partially supported by the UKRI Engineering and Physical Sciences Research Council (UKRI EPSRC) NowNano Centre for Doctoral Training programs (EP/K016946/1 and EP/M010619/1), and the European Union (EU) 7th and 8th Framework Programmes for Research and Technological Development, Graphene Flagship project (FP7-ICT-2013-FET-F-604391 and H2020-FET-696656–Graphene Core 1). We gratefully acknowledge the Centre National de la Recherche Scientifique (CNRS), the International Center for Frontier Research in Chemistry (icFRC), and financial support from the Agence Nationale de la Recherche (ANR) through the LabEx project Chemistry of Complex Systems (ANR-10-LABX-0026_CSC). We would like to acknowledge the staff in the Faculty of Biology, Medicine, and Health at the University of Manchester, particularly Dr. Aleksandr Mironov and Ms. Samantha Forbes from Electron Microscopy Facility for their expert advice and assistance, and the Wellcome Trust for equipment grant support to the Facility. We wish to thank Mr. R. Meadows from the Bioimaging Facility. The Bioimaging Facility microscopes used in this study were purchased with grants from the UKRI Biotechnology and Biological Sciences Research Council (UKRI BBSRC), the Wellcome Trust, and the University of Manchester Strategic Fund. We are grateful to Mr. P. Walker from the Histology Facility for expert advice and assistance in tissue histology and to Dr. N. Hodson from the Bio-AFM Facility for assistance and advice regarding the AFM instrumentation.

## AUTHOR CONTRIBUTIONS

L.N., C.B., and K.K. conceived and executed the overall project. A.F.R. synthesized and L.N. characterized the non-functionalized GO materials. D.J. conducted the

SPECT/CT-related experiments. I.A.V., C. M-M, and A.B. performed the chemical functionalization of the materials, and L.N. characterized the GO materials with DOTA. L.N. and A.F.R. performed the remaining biodistribution and biodegradation experiments. L.N. analyzed all of the results and lead the writing of the manuscript. All of the authors contributed to the writing and editing of the manuscript.

## DECLARATION OF INTERESTS

The authors declare no competing interests.

Received: May 1, 2020
Revised: June 26, 2020
Accepted: July 27, 2020
Published: August 19, 2020

## REFERENCES

1. Ferrari, A.C., Bonaccorso, F., Fal'ko, V., Novoselov, K.S., Roche, S., Bøggild, P., Borini, S., Koppens, F.H.L., Palermo, V., Pugno, N., et al. (2015). Science and technology roadmap for graphene, related two-dimensional crystals, and hybrid systems. Nanoscale *7*, 4598–4810.

2. Novoselov, K.S., Fal'ko, V.I., Colombo, L., Gellert, P.R., Schwab, M.G., and Kim, K. (2012). A roadmap for graphene. Nature *490*, 192–200.

3. Novoselov, K.S., Geim, A.K., Morozov, S.V., Jiang, D., Zhang, Y., Dubonos, S.V., Grigorieva, I.V., and Firsov, A.A. (2004). Electric field effect in atomically thin carbon films. Science *306*, 666–669.

4. Huang, X., Yin, Z., Wu, S., Qi, X., He, Q., Zhang, Q., Yan, Q., Boey, F., and Zhang, H. (2011). Graphene-based materials: synthesis, characterization, properties, and applications. Small *7*, 1876–1902.

5. Dreyer, D.R., Park, S., Bielawski, C.W., and Ruoff, R.S. (2010). The chemistry of graphene oxide. Chem. Soc. Rev. *39*, 228–240.

6. Su, Y., Kravets, V.G., Wong, S.L., Waters, J., Geim, A.K., and Nair, R.R. (2014). Impermeable barrier films and protective coatings based on reduced graphene oxide. Nat. Commun. *5*, 4843.

7. Abraham, J., Vasu, K.S., Williams, C.D., Gopinadhan, K., Su, Y., Cherian, C.T., Dix, J., Prestat, E., Haigh, S.J., Grigorieva, I.V., et al. (2017). Tunable sieving of ions using graphene oxide membranes. Nat. Nanotechnol. *12*, 546–550.

8. Li, F., Jiang, X., Zhao, J., and Zhang, S. (2015). Graphene oxide: a promising nanomaterial for energy and environmental applications. Nano Energy *16*, 488–515.

9. Wang, Y., Yang, J., and Ouyang, D. (2019). Effect of graphene oxide on mechanical properties of cement mortar and its strengthening mechanism. Materials (Basel) *12*, 3753.

10. Bitounis, D., Ali-Boucetta, H., Hong, B.H., Min, D.-H., and Kostarelos, K. (2013). Prospects and challenges of graphene in biomedical applications. Adv. Mater. *25*, 2258–2268.

11. Gurunathan, S., and Kim, J.-H. (2016). Synthesis, toxicity, biocompatibility, and biomedical applications of graphene and graphene-related materials. Int. J. Nanomedicine *11*, 1927–1945.

12. Buelke, C., Alshami, A., Casler, J., Lewis, J., Al-Sayaghi, M., and Hickner, M.A. (2018). Graphene oxide membranes for enhancing water purification in terrestrial and space-born applications: state of the art. Desalination *448*, 113–132.

13. Sanchez, V.C., Jachak, A., Hurt, R.H., and Kane, A.B. (2012). Biological interactions of graphene-family nanomaterials: an interdisciplinary review. Chem. Res. Toxicol. *25*, 15–34.

14. Ellenbecker, M.J., and Tsai, C.S.-J. (2015). Routes of Exposure for Engineered Nanoparticles. In Exposure Assessment and Safety Considerations for Working with Engineered Nanoparticles (John Wiley & Sons), pp. 39–50.

15. International Commission on Radiological Protection (1995). Human Respiratory Tract Model for Radiological Protection (Pergamon Press).

16. Illum, L. (2004). Is nose-to-brain transport of drugs in man a reality? J. Pharm. Pharmacol. *56*, 3–17.

17. Kreyling, W.G., Semmler-Behnke, M., and Möller, W. (2006). Ultrafine particle-lung interactions: does size matter? J. Aerosol Med. *19*, 74–83.

18. Kreyling, W.G., Semmler-Behnke, M., and Möller, W. (2006). Health implications of nanoparticles. J. Nanopart. Res. *8*, 543–562.

19. Oberdörster, G., Elder, A., and Rinderknecht, A. (2009). Nanoparticles and the brain: cause for concern? J. Nanosci. Nanotechnol. *9*, 4996–5007.

20. Schinwald, A., Murphy, F.A., Jones, A., MacNee, W., and Donaldson, K. (2012). Graphene-based nanoplatelets: a new risk to the respiratory system as a consequence of their unusual aerodynamic properties. ACS Nano *6*, 736–746.

21. Bussy, C., Jasim, D., Lozano, N., Terry, D., and Kostarelos, K. (2015). The current graphene safety landscape–a literature mining exercise. Nanoscale *7*, 6432–6435.

22. Rodrigues, A.F., Newman, L., Jasim, D., Mukherjee, S.P., Wang, J., Vacchi, I.A., Ménard-Moyon, C., Bianco, A., Fadeel, B., Kostarelos, K., et al. (2020). Size-dependent pulmonary impact of thin graphene oxide sheets in mice: towards safe-by-design. Adv. Sci. *7*, 1903200.

23. De Lorenzo, A., and Darin, J. (1970). The olfactory neurone and the blood-brain barrier. In Taste and Smell in Vertebrates, G.E.W. Wolfenholme and J. Knight, eds. (Churchill), pp. 151–176.

24. Patchin, E.S., Anderson, D.S., Silva, R.M., Uyeminami, D.L., Scott, G.M., Guo, T., Van Winkle, L.S., and Pinkerton, K.E. (2016). Size-dependent deposition, translocation, and microglial activation of inhaled silver nanoparticles in the rodent nose and brain. Environ. Health Perspect. *124*, 1870–1875.

25. Wang, B., Feng, W.Y., Wang, M., Shi, J.W., Zhang, F., Ouyang, H., Zhao, Y.L., Chai, Z.F., Huang, Y.Y., Xie, Y.N., et al. (2007). Transport of intranasally instilled fine $Fe_2O_3$ particles into the brain: micro-distribution, chemical states, and histopathological observation. Biol. Trace Elem. Res. *118*, 233–243.

26. Oberdörster, G., Sharp, Z., Atudorei, V., Elder, A., Gelein, R., Kreyling, W., and Cox, C. (2004). Translocation of inhaled ultrafine particles to the brain. Inhal. Toxicol. *16*, 437–445.

27. Wang, J., Chen, C., Liu, Y., Jiao, F., Li, W., Lao, F., Li, Y., Li, B., Ge, C., Zhou, G., et al. (2008). Potential neurological lesion after nasal instillation of $TiO_{(2)}$ nanoparticles in the anatase and rutile crystal phases. Toxicol. Lett. *183*, 72–80.

28. Elder, A., Gelein, R., Silva, V., Feikert, T., Opanashuk, L., Carter, J., Potter, R., Maynard, A., Ito, Y., Finkelstein, J., and Oberdörster, G. (2006). Translocation of inhaled ultrafine manganese oxide particles to the central nervous system. Environ. Health Perspect. *114*, 1172–1178.

29. Zhuang, X., Xiang, X., Grizzle, W., Sun, D., Zhang, S., Axtell, R.C., Ju, S., Mu, J., Zhang, L.,

Steinman, L., et al. (2011). Treatment of brain inflammatory diseases by delivering exosome encapsulated anti-inflammatory drugs from the nasal region to the brain. Mol. Ther. *19*, 1769–1779.

30. Maher, B.A., Ahmed, I.A.M., Karloukovski, V., MacLaren, D.A., Foulds, P.G., Allsop, D., Mann, D.M.A., Torres-Jardón, R., and Calderon-Garciduenas, L. (2016). Magnetite pollution nanoparticles in the human brain. Proc. Natl. Acad. Sci. USA *113*, 10797–10801.

31. De Lorenzo, A.J. (1957). Electron microscopic observations of the olfactory mucosa and olfactory nerve. J. Biophys. Biochem. Cytol. *3*, 839–850.

32. Thorne, R.G., Pronk, G.J., Padmanabhan, V., and Frey, W.H., 2nd (2004). Delivery of insulin-like growth factor-I to the rat brain and spinal cord along olfactory and trigeminal pathways following intranasal administration. Neuroscience *127*, 481–496.

33. Hunter, D.D., and Dey, R.D. (1998). Identification and neuropeptide content of trigeminal neurons innervating the rat nasal epithelium. Neuroscience *83*, 591–599.

34. Frey, W.H., Liu, J., Chen, X., Thorne, R.G., Fawcett, J.R., Ala, T.A., and Rahman, Y.-E. (1997). Delivery of $^{125}$I-NGF to the brain via the olfactory route. Drug Deliv. *4*, 87–92.

35. Shepherd, G. (1994). Neurobiology (Oxford University Press).

36. Illum, L. (2000). Transport of drugs from the nasal cavity to the central nervous system. Eur. J. Pharm. Sci. *11*, 1–18.

37. Pardridge, W.M. (2007). Blood-brain barrier delivery. Drug Discov. Today *12*, 54–61.

38. Loureiro, J.A., Gomes, B., Coelho, M.A., do Carmo Pereira, M., and Rocha, S. (2014). Targeting nanoparticles across the blood-brain barrier with monoclonal antibodies. Nanomedicine (Lond.) *9*, 709–722.

39. Girish, C.M., Sasidharan, A., Gowd, G.S., Nair, S., and Koyakutty, M. (2013). Confocal Raman imaging study showing macrophage mediated biodegradation of graphene in vivo. Adv. Healthc. Mater. *2*, 1489–1500.

40. Nunes, A., Bussy, C., Gherardini, L., Meneghetti, M., Herrero, M.A., Bianco, A., Prato, M., Pizzorusso, T., Al-Jamal, K.T., and Kostarelos, K. (2012). In vivo degradation of functionalized carbon nanotubes after stereotactic administration in the brain cortex. Nanomedicine (Lond.) *7*, 1485–1494.

41. Shvedova, A.A., Kapralov, A.A., Feng, W.H., Kisin, E.R., Murray, A.R., Mercer, R.R., St Croix, C.M., Lang, M.A., Watkins, S.C., Konduru, N.V., et al. (2012). Impaired clearance and enhanced pulmonary inflammatory/fibrotic response to carbon nanotubes in myeloperoxidase-deficient mice. PLOS ONE *7*, e30923.

42. Elgrabli, D., Dachraoui, W., Ménard-Moyon, C., Liu, X.J., Bégin, D., Bégin-Colin, S., Bianco, A., Gazeau, F., and Alloyeau, D. (2015). Carbon nanotube degradation in macrophages: live nanoscale monitoring and understanding of biological pathway. ACS Nano *9*, 10113–10124.

43. Newman, L., Jasim, D.A., Prestat, E., Lozano, N., de Lázaro, I., Nam, Y., Assas, B.M., Pennock, J., Haigh, S.J., Bussy, C., and Kostarelos, K. (2020). Splenic capture and in vivo intracellular biodegradation of thin, biological-grade graphene oxide sheets. ACS Nano. https://doi.org/10.1021/acsnano.0c03438.

44. Bussy, C., Hadad, C., Prato, M., Bianco, A., and Kostarelos, K. (2016). Intracellular degradation of chemically functionalized carbon nanotubes using a long-term primary microglial culture model. Nanoscale *8*, 590–601.

45. Goode, A.E., Gonzalez Carter, D.A., Motskin, M., Pienaar, I.S., Chen, S., Hu, S., Ruenraroengsak, P., Ryan, M.P., Shaffer, M.S.P., Dexter, D.T., and Porter, A.E. (2015). High resolution and dynamic imaging of biopersistence and bioreactivity of extra and intracellular MWNTs exposed to microglial cells. Biomaterials *70*, 57–70.

46. Russier, J., Oudjedi, L., Piponnier, M., Bussy, C., Prato, M., Kostarelos, K., Lounis, B., Bianco, A., and Cognet, L. (2017). Direct visualization of carbon nanotube degradation in primary cells by photothermal imaging. Nanoscale *9*, 4642–4645.

47. Mukherjee, S.P., Lozano, N., Kucki, M., Del Rio-Castillo, A.E., Newman, L., Vázquez, E., Kostarelos, K., Wick, P., and Fadeel, B. (2016). Detection of endotoxin contamination of graphene based materials using the TNF-α expression test and guidelines for endotoxin-free graphene oxide production. PLOS ONE *11*, e0166816.

48. Rodrigues, A.F., Newman, L., Lozano, N., Mukherjee, S.P., Fadeel, B., Bussy, C., and Kostarelos, K. (2018). A blueprint for the synthesis and characterisation of thin graphene oxide with controlled lateral dimensions for biomedicine. 2D Mater. *5*, 035020.

49. Peters, A., and Pope, C.A., 3rd (2002). Cardiopulmonary mortality and air pollution. Lancet *360*, 1184–1185.

50. Mittal, D., Ali, A., Md, S., Baboota, S., Sahni, J.K., and Ali, J. (2014). Insights into direct nose to brain delivery: current status and future perspective. Drug Deliv. *21*, 75–86.

51. Vacchi, I.A., Spinato, C., Raya, J., Bianco, A., and Ménard-Moyon, C. (2016). Chemical reactivity of graphene oxide towards amines elucidated by solid-state NMR. Nanoscale *8*, 13714–13721.

52. Jasim, D.A., Ménard-Moyon, C., Bégin, D., Bianco, A., and Kostarelos, K. (2015). Tissue distribution and urinary excretion of intravenously administered chemically functionalized graphene oxide sheets. Chem. Sci. (Camb.) *6*, 3952–3964.

53. Li, Y., Feng, L., Shi, X., Wang, X., Yang, Y., Yang, K., Liu, T., Yang, G., and Liu, Z. (2014). Surface coating-dependent cytotoxicity and degradation of graphene derivatives: towards the design of non-toxic, degradable nano-graphene. Small *10*, 1544–1554.

54. Li, J.L., Kudin, K.N., McAllister, M.J., Prud'homme, R.K., Aksay, I.A., and Car, R. (2006). Oxygen-driven unzipping of graphitic materials. Phys. Rev. Lett. *96*, 176101.

55. Sun, T., and Fabris, S. (2012). Mechanisms for oxidative unzipping and cutting of graphene. Nano Lett. *12*, 17–21.

56. Zhang, S., Yang, K., Feng, L., and Liu, Z. (2011). In vitro and in vivo behaviors of dextran functionalized graphene. Carbon *49*, 4040–4049.

57. Ferrari, A.C., and Robertson, J. (2000). Interpretation of Raman spectra of disordered and amorphous carbon. Phys. Rev. B Condens. Matter Mater. Phys. *61*, 14095–14107.

58. Du, L., Wu, S., Li, Y., Zhao, X., Ju, X., and Wang, Y. (2014). Cytotoxicity of PEGylated graphene oxide on lymphoma cells. Biomed. Mater. Eng. *24*, 2135–2141.

59. Banerjee, T., Mitra, S., Kumar Singh, A., Kumar Sharma, R., and Maitra, A. (2002). Preparation, characterization and biodistribution of ultrafine chitosan nanoparticles. Int. J. Pharm. *243*, 93–105.

60. Pressly, E.D., Rossin, R., Hagooly, A., Fukukawa, K., Messmore, B.W., Welch, M.J., Wooley, K.L., Lamm, M.S., Hule, R.A., Pochan, D.J., and Hawker, C.J. (2007). Structural effects on the biodistribution and positron emission tomography (PET) imaging of well-defined (64)Cu-labeled nanoparticles comprised of amphiphilic block graft copolymers. Biomacromolecules *8*, 3126–3134.

61. Yang, K., Wan, J., Zhang, S., Zhang, Y., Lee, S.-T., and Liu, Z. (2011). In vivo pharmacokinetics, long-term biodistribution, and toxicology of PEGylated graphene in mice. ACS Nano *5*, 516–522.

62. Cornelissen, B., Able, S., Kersemans, V., Waghorn, P.A., Myhra, S., Jurkshat, K., Crossley, A., and Vallis, K.A. (2013). Nanographene oxide-based radioimmunoconstructs for in vivo targeting and SPECT imaging of HER2-positive tumors. Biomaterials *34*, 1146–1154.

63. Wick, P., Louw-Gaume, A.E., Kucki, M., Krug, H.F., Kostarelos, K., Fadeel, B., Dawson, K.A., Salvati, A., Vázquez, E., Ballerini, L., et al. (2014). Classification framework for graphene-based materials. Angew. Chem. Int. Ed. Engl. *53*, 7714–7718.

64. Hopkins, L.E., Patchin, E.S., Chiu, P.-L., Brandenberger, C., Smiley-Jewell, S., and Pinkerton, K.E. (2014). Nose-to-brain transport of aerosolised quantum dots following acute exposure. Nanotoxicology *8*, 885–893.

65. Kristensson, K., and Olsson, Y. (1971). Uptake of exogenous proteins in mouse olfactory cells. Acta Neuropathol. *19*, 145–154.

66. Jasim, D.A., Murphy, S., Newman, L., Mironov, A., Prestat, E., McCaffrey, J., Ménard-Moyon, C., Rodrigues, A.F., Bianco, A., Haigh, S., et al. (2016). The effects of extensive glomerular filtration of thin graphene oxide sheets on kidney physiology. ACS Nano *10*, 10753–10767.

67. Zhang, X., Yin, J., Peng, C., Hu, W., Zhu, Z., Li, W., Fan, C., and Huang, Q. (2011). Distribution

and biocompatibility studies of graphene oxide in mice after intravenous administration. Carbon *49*, 986–995.

68. Sasidharan, A., Swaroop, S., Koduri, C.K., Girish, C.M., Chandran, P., Panchakarla, L.S., Somasundaram, V.H., Gowd, G.S., Nair, S., and Koyakutty, M. (2015). Comparative in vivo toxicity, organ biodistribution and immune response of pristine, carboxylated and PEGylated few-layer graphene sheets in swiss albino mice: a three month study. Carbon *95*, 511–524.

69. Wang, Y., Aun, R., and Tse, F.L. (1998). Brain uptake of dihydroergotamine after intravenous and nasal administration in the rat. Biopharm. Drug Dispos. *19*, 571–575.

70. Chow, H.S., Chen, Z., and Matsuura, G.T. (1999). Direct transport of cocaine from the nasal cavity to the brain following intranasal cocaine administration in rats. J. Pharm. Sci. *88*, 754–758.

71. Lochhead, J.J., Wolak, D.J., Pizzo, M.E., and Thorne, R.G. (2015). Rapid transport within cerebral perivascular spaces underlies widespread tracer distribution in the brain after intranasal administration. J. Cereb. Blood Flow Metab. *35*, 371–381.

72. Stevenson, B.R., Anderson, J.M., and Bullivant, S. (1988). The epithelial tight junction: structure, function and preliminary biochemical characterization. Mol. Cell. Biochem. *83*, 129–145.

73. Costantino, H.R., Illum, L., Brandt, G., Johnson, P.H., and Quay, S.C. (2007). Intranasal delivery: physicochemical and therapeutic aspects. Int. J. Pharm. *337*, 1–24.

74. van Woensel, M., Wauthoz, N., Rosière, R., Amighi, K., Mathieu, V., Lefranc, F., van Gool, S.W., and de Vleeschouwer, S. (2013). Formulations for intranasal delivery of pharmacological agents to combat brain disease: a new opportunity to tackle GBM? Cancers (Basel) *5*, 1020–1048.

75. Caggiano, M., Kauer, J.S., and Hunter, D.D. (1994). Globose basal cells are neuronal progenitors in the olfactory epithelium: a lineage analysis using a replication-incompetent retrovirus. Neuron *13*, 339–352.

76. Geraci, C., Heidel, D., Sayes, C., Hodson, L., Schulte, P., Eastlake, A., and Brenner, S. (2015). Perspectives on the design of safer nanomaterials and manufacturing processes. J. Nanopart. Res. *17*, 366.

77. Ali, M.S., and Pearson, J.P. (2007). Upper airway mucin gene expression: a review. Laryngoscope *117*, 932–938.

78. Lai, S.K., Wang, Y.-Y., and Hanes, J. (2009). Mucus-penetrating nanoparticles for drug and gene delivery to mucosal tissues. Adv. Drug Deliv. Rev. *61*, 158–171.

79. Wu, J., Ding, T., and Sun, J. (2013). Neurotoxic potential of iron oxide nanoparticles in the rat brain striatum and hippocampus. Neurotoxicology *34*, 243–253.

80. Iliff, J.J., Wang, M., Liao, Y., Plogg, B.A., Peng, W., Gundersen, G.A., Benveniste, H., Vates, G.E., Deane, R., Goldman, S.A., et al. (2012). A paravascular pathway facilitates CSF flow through the brain parenchyma and the clearance of interstitial solutes, including amyloid β. Sci. Transl. Med. *4*, 147ra111.

81. Hadaczek, P., Yamashita, Y., Mirek, H., Tamas, L., Bohn, M.C., Noble, C., Park, J.W., and Bankiewicz, K. (2006). The "perivascular pump" driven by arterial pulsation is a powerful mechanism for the distribution of therapeutic molecules within the brain. Mol. Ther. *14*, 69–78.

82. Yan, L., Wang, H., Jiang, Y., Liu, J., Wang, Z., Yang, Y., Huang, S., and Huang, Y. (2013). Cell-penetrating peptide-modified PLGA nanoparticles for enhanced nose-to-brain macromolecular delivery. Macromol. Res. *21*, 435–441.

83. Quignon, P., Kirkness, E., Cadieu, E., Touleimat, N., Guyon, R., Renier, C., Hitte, C., André, C., Fraser, C., and Galibert, F. (2003). ). Comparison of the canine and human olfactory receptor gene repertoires. Genome Biol. *4*, R80.

84. Hutter, E., Boridy, S., Labrecque, S., Lalancette-Hébert, M., Kriz, J., Winnik, F.M., and Maysinger, D. (2010). Microglial response to gold nanoparticles. ACS Nano *4*, 2595–2606.

85. Wang, Y., Wang, B., Zhu, M.-T., Li, M., Wang, H.-J., Wang, M., Ouyang, H., Chai, Z.-F., Feng, W.-Y., and Zhao, Y.-L. (2011). Microglial activation, recruitment and phagocytosis as linked phenomena in ferric oxide nanoparticle exposure. Toxicol. Lett. *205*, 26–37.

86. Bussy, C., Al-Jamal, K.T., Boczkowski, J., Lanone, S., Prato, M., Bianco, A., and Kostarelos, K. (2015). Microglia determine brain region-specific neurotoxic responses to chemically functionalized carbon nanotubes. ACS Nano *9*, 7815–7830.

87. Nicolete, R., dos Santos, D.F., and Faccioli, L.H. (2011). The uptake of PLGA micro or nanoparticles by macrophages provokes distinct in vitro inflammatory response. Int. Immunopharmacol. *11*, 1557–1563.

88. Rauti, R., Medelin, M., Newman, L., Vranic, S., Reina, G., Bianco, A., Prato, M., Kostarelos, K., and Ballerini, L. (2019). Graphene oxide flakes tune excitatory neurotransmission in vivo by targeting hippocampal synapses. Nano Lett. *19*, 2858–2870.

89. Bedussi, B., van Lier, M.G.J.T.B., Bartstra, J.W., de Vos, J., Siebes, M., VanBavel, E., and Bakker, E.N.T.P. (2015). Clearance from the mouse brain by convection of interstitial fluid towards the ventricular system. Fluids Barriers CNS *12*, 23.

90. Xie, L., Kang, H., Xu, Q., Chen, M.J., Liao, Y., Thiyagarajan, M., O'Donnell, J., Christensen, D.J., Nicholson, C., Iliff, J.J., et al. (2013). Sleep drives metabolite clearance from the adult brain. Science *342*, 373–377.

91. Ding, Y., Tian, R., Yang, Z., Chen, J., and Lu, N. (2017). NADPH oxidase-dependent degradation of single-walled carbon nanotubes in macrophages. J. Mater. Sci. Mater. Med. *28*, 7.

92. Bhattacharya, K., Mukherjee, S.P., Gallud, A., Burkert, S.C., Bistarelli, S., Bellucci, S., Bottini, M., Star, A., and Fadeel, B. (2016). Biological interactions of carbon-based nanomaterials: from coronation to degradation. Nanomedicine (Lond.) *12*, 333–351.

93. Chen, M., Qin, X., and Zeng, G. (2017). Biodegradation of carbon nanotubes, graphene, and their derivatives. Trends Biotechnol. *35*, 836–846.

94. Lucchese, M.M., Stavale, F., Ferreira, E.H.M., Vilani, C., Moutinho, M.V.O., Capaz, R.B., Achete, C.A., and Jorio, A. (2010). Quantifying ion-induced defects and Raman relaxation length in graphene. Carbon *48*, 1592–1597.

95. Zhang, M., Yang, M., Bussy, C., Iijima, S., Kostarelos, K., and Yudasaka, M. (2015). Biodegradation of carbon nanohorns in macrophage cells. Nanoscale *7*, 2834–2840.

96. Kagan, V.E., Konduru, N.V., Feng, W., Allen, B.L., Conroy, J., Volkov, Y., Vlasova, I.I., Belikova, N.A., Yanamala, N., Kapralov, A., et al. (2010). Carbon nanotubes degraded by neutrophil myeloperoxidase induce less pulmonary inflammation. Nat. Nanotechnol. *5*, 354–359.

97. Lu, N., Li, J., Tian, R., and Peng, Y.-Y. (2014). Binding of human serum albumin to single-walled carbon nanotubes activated neutrophils to increase production of hypochlorous acid, the oxidant capable of degrading nanotubes. Chem. Res. Toxicol. *27*, 1070–1077.

98. Mukherjee, S.P., Gliga, A.R., Lazzaretto, B., Brandner, B., Fielden, M., Vogt, C., Newman, L., Rodrigues, A.F., Shao, W., Fournier, P.M., et al. (2018). Graphene oxide is degraded by neutrophils and the degradation products are non-genotoxic. Nanoscale *10*, 1180–1188.

99. Osmond-McLeod, M.J., Poland, C.A., Murphy, F., Waddington, L., Morris, H., Hawkins, S.C., Clark, S., Aitken, R., McCall, M.J., and Donaldson, K. (2011). Durability and inflammogenic impact of carbon nanotubes compared with asbestos fibres. Part. Fibre Toxicol. *8*, 15.

100. Burkholder, T., Foltz, C., Karlsson, E., Linton, C.G., and Smith, J.M. (2012). Health evaluation of experimental laboratory mice. Curr. Protoc. Mouse Biol. *2*, 145–165.

101. Kotchey, G.P., Hasan, S.A., Kapralov, A.A., Ha, S.H., Kim, K., Shvedova, A.A., Kagan, V.E., and Star, A. (2012). A natural vanishing act: the enzyme-catalyzed degradation of carbon nanomaterials. Acc. Chem. Res. *45*, 1770–1781.